Multi-relaxation time lattice Boltzmann simulation of inertial secondary flow in a curved microchannel*

Sun Dong-Ke(孙东科)†, Xiang Nan(项 楠), Jiang Di(姜 迪), Chen Ke(陈 科), Yi Hong(易 红), and Ni Zhong-Hua(倪中华)‡

Jiangsu Key Laboratory for Design and Manufacture of Micro-Nano Biomedical Instruments, School of Mechanical Engineering, Southeast University, Nanjing 211189, *China*

(Received 17 February 2013; revised manuscript received 13 March 2013)

The inertial secondary flow is particularly important for hydrodynamic focusing and particle manipulation in biomedical research. In this paper, the development of the inertial secondary flow structure in a curved microchannel was investigated by the multi relaxation time lattice Boltzmann equation model with a force term. The numerical results indicate that the viscous and inertial competition dominates the development of secondary flow structure development. The Reynolds number, Dean number, and the cross section aspect ratio influence significantly on the development of the secondary vortexes. Both the intensity of secondary flow and the distance between the normalized vortex centers are functions of Dean numbers but independent of channel curvature radius. In addition, the competition mechanism between the viscous and inertial effects were discussed by performing the particle focusing experiments. The present investigation provides an improved understanding of the development of inertial secondary flows in curved microchannels.

Keywords: lattice Boltzmann method, multi relaxation time, microchannel, inertial secondary flow

PACS: 47.27.nd, 47.11.–j, 04.60.Nc **DOI:** 10.1088/1674-1056/22/11/114704

1. Introduction

Hydrodynamic focusing based on inertial microfluidics are becoming a utilized as a high-throughput technique of particles manipulation. It has been employed in wide applications as varied as cell sorting, chemical and biochemical analysis, on-chip flow cytometry, chemical reactors, single molecule detection, size-selective separation, and others.[1,2] It is known that the principle of hydrodynamic focusing is based on the theoretical analysis of inertial secondary flow and viscous shear induced lift force.[3,4] The secondary flow, which arises when the fluid flows in a curved channel with a small radius of curvature, is a relatively minor flow imposed on the primary flow.[5] As it has helical streamlines, the secondary flow is favorably used to separate micro particles in recent years. Although experimental studies showed the feasibility of hydrodynamic focusing by using a device with various curved channels, a decent understanding of the inertial secondary flow and the lift force evolution is still insufficient because of its complexity. Knowledge regarding the development of fluid flow in curved microchannels is particularly important for optimizing equipment design and operation.

With the developing computational power available nowadays, numerical simulation has become an indispensable method to study channel flows[6,7] and especially the fluid flows in curved microchannels.[8–10] Ookawara *et al.*[8] carried out a numerical study on the development of particle concentration distributions in an arc microchannel by employing the Eulerian–Eulerian multiphase approach. They analyzed the development of Dean vortices, lift force, and particle concentration profiles over the channel cross-sectional plane. Yoon *et al.*[9] performed a numerical study of the Dean vortices in a U-shape microchannel. They stated that the zero velocities on the cross section were always positioned at the same normalized height of 0.27 and 0.72 regardless of the different Reynolds numbers (0.27–0.72 rule). However, the 0.27–0.72 rule cannot be satisfied when the Reynolds number becomes higher, as found in our recent investagation. Mao *et al.*[10] performed a three-dimensional (3D) simulation of viscous flow in a quarter annular microchannel by using commercial software (CFD-ACE+, ESI-CFD). It demonstrates the reliability of numerical simulation for microchannel flow. However, the underlying competition mechanism between the viscous shear and the inertial effects on fluid has not been fully addressed in detail. In the last decades, the lattice Boltzmann method (LBM) has become a relatively newly developed simulation technique for fluid systems,[11–14] especially for micro scale fluid flows.[15,16] It has shown great potential in dealing with fluid flow with a complex geometry boundary with better computational accuracy and numerical stability than traditional methods.[17–19] Therefore, it is straightforward to employ the LBM to investigate the complex mechanism of secondary flows in curved microchannels.

*Project supported by the National Basic Research Program of China (Grant No. 2011CB707601), the National Natural Science Foundation of China (Grant Nos. 51306037 and 51375089), and the National Science Foundation for Post-doctoral Scientists of China (Grant No. 2012M511647).

†Corresponding author. E-mail: dongke.sun@gmail.com

‡Corresponding author. E-mail: nzh2003@seu.edu.cn

© 2013 Chinese Physical Society and IOP Publishing Ltd

The intention of the present work is to investigate the development of secondary flow structures and the competition mechanism of viscous/inertial effects in curved microchannel flows. Firstly, we introduce the multi relaxation time – lattice Boltzmann equation (MRT-LBE) model with a force term,[12,13] and then validate the model and algorithm by taking the lid-driven cavity flow as a benchmark. Subsequently, the characteristic velocity profiles on the channel cross-sectional plane under various driven forces have been analyzed quantitatively. Next, the competition mechanism between the viscous and inertial effects are discussed by analyzing the particle focusing experimental observations. A brief summary is given in the last section.

2. Model and algorithm

2.1. Multi relaxation time lattice Boltzmann equation model

The evolution equation for the MRT-LBE model with a force term of Q velocities $\boldsymbol{e}_i$ on a D-dimensional lattice can be expressed as[12,13]

$$\begin{aligned}&\boldsymbol{f}(\boldsymbol{x}+\boldsymbol{e}_i\Delta t, t+\Delta t)-\boldsymbol{f}(\boldsymbol{x},t)\\ &=-\boldsymbol{M}^{-1}\cdot\hat{\boldsymbol{S}}\cdot[\boldsymbol{m}(\boldsymbol{x},t)-\boldsymbol{m}^{\mathrm{eq}}(\boldsymbol{x},t)]+\boldsymbol{F}(\boldsymbol{x},t),\end{aligned}\tag{1}$$

where $\boldsymbol{M}$ is a $Q\times Q$ linear transformation matrix which defines the mapping between the particle distribution function $\boldsymbol{f}$ to the velocity moment $\boldsymbol{m}$

$$\boldsymbol{m}=\boldsymbol{M}\cdot\boldsymbol{f},\quad \boldsymbol{f}=\boldsymbol{M}^{-1}\cdot\boldsymbol{m},\tag{2}$$

$\hat{\boldsymbol{S}}$ is a non-negative $Q\times Q$ diagonal relaxation matrix composed of relaxation time $(s_0,s_1,\ldots,s_{Q-1})$, $\boldsymbol{m}^{\mathrm{eq}}$ is the equilibrium values of the velocity moments, and the force term $\boldsymbol{F}$ represents the contribution of the volumetric body force on fluids to the distribution functions. The symbols $\boldsymbol{f}$, $\boldsymbol{F}$, $\boldsymbol{m}$, and $\boldsymbol{m}^{\mathrm{eq}}$ in Eq. (1) are three column matrices which are defined as

$$\boldsymbol{f}(\boldsymbol{x},t)\equiv[f_0(\boldsymbol{x},t),(f_1(\boldsymbol{x},t),\ldots,f_{Q-1}(\boldsymbol{x},t)]^{\mathrm{T}},\tag{3}$$

$$\boldsymbol{F}(\boldsymbol{x},t)\equiv[F_0(\boldsymbol{x},t),(F_1(\boldsymbol{x},t),\ldots,F_{Q-1}(\boldsymbol{x},t)]^{\mathrm{T}},\tag{4}$$

$$\boldsymbol{m}(\boldsymbol{x},t)\equiv[m_0(\boldsymbol{x},t),(m_1(\boldsymbol{x},t),\ldots,m_{Q-1}(\boldsymbol{x},t)]^{\mathrm{T}},\tag{5}$$

$$\boldsymbol{m}^{\mathrm{eq}}(\boldsymbol{x},t)\equiv[m_0^{\mathrm{eq}}(\boldsymbol{x},t),(m_1^{\mathrm{eq}}(\boldsymbol{x},t),\ldots,m_{Q-1}^{\mathrm{eq}}(\boldsymbol{x},t)]^{\mathrm{T}},\tag{6}$$

where the superscript T and eq denote the transpose operator and the equilibrium of the fluids, respectively.

For the sake of numerical stability and calculation accuracy, we adopt the D3Q19 model with the following discrete velocities $\boldsymbol{e}_i$:

$$[\boldsymbol{e}_i,i=0,\ldots,18]=\begin{bmatrix}0,&c,&-c,&0,&0,&0,&0,&c,&-c,&c,&-c,&c,&-c,&c,&-c,&0,&0,&0,&0\\0,&0,&0,&c,&-c,&0,&0,&c,&-c,&-c,&c,&0,&0,&0,&0,&c,&-c,&c,&-c\\0,&0,&0,&0,&0,&c,&-c,&0,&0,&0,&0,&c,&-c,&-c,&c,&c,&-c,&-c,&c\end{bmatrix},\tag{7}$$

where the lattice speed $c\equiv\Delta x/\Delta t$. The resulting moments $\boldsymbol{m}$ are labelled as

$$\boldsymbol{m}=[\rho,e,\varepsilon,j_x,q_x,j_y,q_y,j_z,q_z,3p_{xx},3\pi_{xx},p_{ww},\pi_{ww},p_{xy},p_{yz},p_{zx},t_x,t_y,t_z]^{\mathrm{T}},\tag{8}$$

in which ρ is the mass density, j_x,j_y,j_z are the x,y,z components of the flow momentum $\boldsymbol{j}$, and $\boldsymbol{j}\equiv\rho(u_x,u_y,u_z)$. The corresponding equilibrium moments $\boldsymbol{m}^{\mathrm{eq}}$ are[12]

$$\begin{aligned}\boldsymbol{m}^{\mathrm{eq}}=[&\rho,-\rho(11-19u^2),\rho(\alpha+\beta u^2),j_x,-\frac{2}{3}j_x,j_y,\\&-\frac{2}{3}j_y,j_z,-\frac{2}{3}j_z,\frac{1}{\rho_0}(2j_x^2-j_y^2-j_z^2),\\&\frac{\gamma}{\rho_0}(2j_x^2-j_y^2-j_z^2),\frac{1}{\rho_0}(j_y^2-j_z^2),\frac{\gamma}{\rho_0}(j_y^2-j_z^2),\\&\frac{1}{\rho_0}j_xj_y,\frac{1}{\rho_0}j_yj_z,\frac{1}{\rho_0}j_zj_x,0,0,0]^{\mathrm{T}},\end{aligned}\tag{9}$$

where u is the magnitude of flow velocity, $u=\sqrt{u_x^2+u_y^2+u_z^2}$, and α, β, γ are free parameters. In the present work, we set $\alpha=3$, $\beta=-5.5$, and $\gamma=-0.5$. With the above sequence of moments, the diagonal matrix $\hat{\boldsymbol{S}}$ is

$$\begin{aligned}\hat{\boldsymbol{S}}=\mathrm{diag}(&0,s_e,s_\varepsilon,0,s_q,0,s_q,0,\\&s_q,s_\nu,s_\pi,s_\nu,s_\pi,s_\nu,s_\nu,s_\nu,s_t,s_t,s_t),\end{aligned}\tag{10}$$

In which, s_ν and s_e are determined by the kinematic viscosity ν and the bulk viscosity ζ according to

$$\nu=\frac{1}{3}\left(\frac{1}{s_\nu}-\frac{1}{2}\right)c\Delta x,\tag{11}$$

$$\zeta=\frac{2}{9}\left(\frac{1}{s_e}-\frac{1}{2}\right)c\Delta x.\tag{12}$$

The values of other elements s_ε, s_q, s_π, and s_t can be chosen more flexibly in the range $(0,2)$. In the present study, we set $s_e=1.19$, $s_\varepsilon=1.0$, $s_q=1.2$, $s_\pi=1.98$, and $s_t=0.98$.

2.2. Numerical procedure

From an algorithmic point of view, the MRT-LBE formulation is implemented in two elementary steps: (i) the relaxation step in which the collision operator is applied to the particle distribution, and (ii) the streaming step in which updated particle populations are propagated to the neighbouring nodes. Therefore, equation (1) may be split into

$$\widetilde{\boldsymbol{f}}(\boldsymbol{x},t)=\boldsymbol{M}^{-1}\cdot\left(\boldsymbol{m}(\boldsymbol{x},t)-\hat{\boldsymbol{S}}\cdot[\boldsymbol{m}(\boldsymbol{x},t)-\boldsymbol{m}^{\mathrm{eq}}(\boldsymbol{x},t)]\right)\tag{13}$$

and

$$\boldsymbol{f}(\boldsymbol{x}+\boldsymbol{e}_i\Delta t, t+\Delta t) = \widetilde{\boldsymbol{f}}(\boldsymbol{x},t) + \boldsymbol{F}(\boldsymbol{x},t), \tag{14}$$

where equation (13) describes the relaxation step and equation (14) is the streaming step, respectively. Thus, The numerical procedure of present MRT-LBE model is summarized as follows.

(I) Initialization: all elements of $\boldsymbol{m}$ are initialized by setting them equal to their equilibrium value $\boldsymbol{m}^{\rm eq}$ which can be determined by Eq. (9) with the initial constant density and the zero velocity.

(II) Relaxation step: with the known moments $\boldsymbol{m}$ and $\boldsymbol{m}^{\rm eq}$, the relaxation step is conducted based on Eq. (13).

(III) Streaming step: the streaming step is performed based on Eq. (14), during which the macroscopic density and velocity of fluid are computed.

(IV) Boundary treatment: inlet, outlet or side boundary conditions are operated by using a specified treatment scheme.

(V) Proceed through the next time-step starting at step (II) until the specified precision is satisfied.

2.3. Algorithm validation

In order to validate and evaluate the present numerical model and computer program, the incompressible lid-driven flow in a cubic cavity ($1.0\times1.0\times1.0$) whose top wall moves with a uniform velocity was considered. For the present cavity flow shown in Fig. 1. There are two types of boundary condition. One is the top lid whose moving velocity is a constant, i.e., $u_{\rm top}=$ const, and the other is the stationary boundary along the remaining five cavity walls. The non-equilibrium extrapolation scheme[20] is employed to determine the unknown particle distribution functions along the top boundary. The other is the five fixed walls of the cavity, where the half-way bounce-back scheme[12] is applied to subject to the non-slip boundary condition. The Reynolds number is defined as $Re = u_{\rm top}L/\nu$, where L is the side length of the cubic, and ν is the kinematic viscosity.

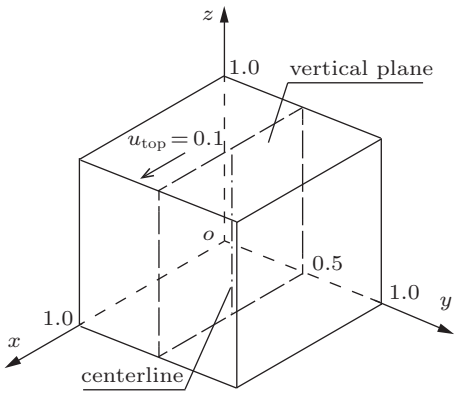


Fig. 1. Sketch of the lid-driven cubic cavity flow.

In the present work, the driven velocity is fixed $u_{\rm top}=0.1$, and Re is set by varying ν. The uniform Cartesian meshes of $50\times50\times50$ and $100\times100\times100$ are employed in the simulation. We consider a Re range of 100 ($\nu=0.001$), 400 ($\nu=0.00025$), and 1000 ($\nu=0.0001$) for which steady transversal vortices are expected to be present. The u-velocity component distribution on the vertical plane centerline has been used as a measure of solution accuracy for the 3D lid-driven cavity benchmark. The computed results from the present simulation are shown in Fig. 2. The present solution is in good agreement with the results of Jiang *et al.*[21] and Wong *et al.*[22] The negative peak velocities on the vertical centerline are listed in Table 1. The maximum difference between the present simulation and Wong's is no more than 11.7% at the peak value in the case of $Re=1000$ and $50\times50\times50$ mesh. As the mesh size increases to $100\times100\times100$, the maximum difference decreases to no more than 5.80% for the same case.

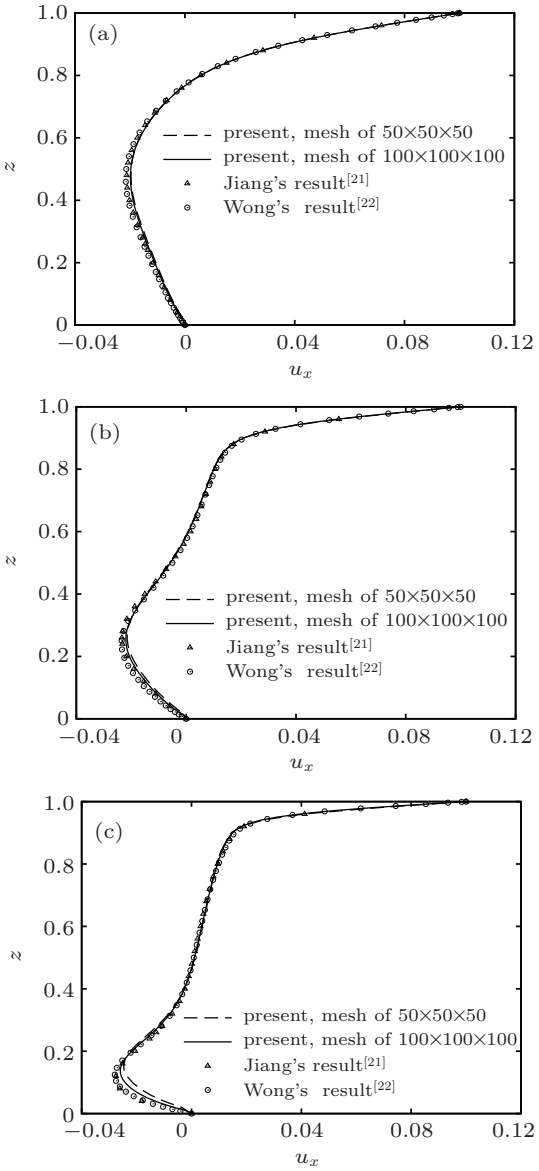


Fig. 2. Velocity profiles on the centerline of vertical plane at $Re=$ (a) 100, (b) 400, and (c) 1000 with uniform meshes of $50\times50\times50$ and $100\times100\times100$.

Table 1. Comparision between the present simulation with the results in references for the negative peak velocity on the vertical centerline at $Re = 100$, 400, and 1000.

Re	Negative peak velocity					
	Jiang *et al.*[21]	Wong *et al.*[22]	Present simulation		Relative difference	
			mesh of $50\times50\times50$	mesh of $100\times100\times100$	Maximum	Minimum
100	−0.2120	−0.2154	−0.1957	−0.1997	9.15%	5.80%
400	−0.2341	−0.2349	−0.2184	−0.2210	7.02%	5.60%
1000	−0.2754	−0.2792	−0.2464	−0.2598	11.7%	5.66%

3. Results and discussion

3.1. Problem description

We next investigate the flow structure development with various driven forces in an annular microchannel. A schematic view of the flow geometry, coordinate system, and computational domain of the problem is illustrated in Fig. 3. Incompressible flow with constant fluid density ρ and constant kinematic viscosity ν is assumed. A Cartesian coordinate system (x,y,z) is applied to describe the flow, where the x,y axis are aligned on the horizontal plane, the z axis is aligned with the depth-direction of the channel. The origin of the coordinates is chosen to be the center point of the bottom plane, as shown in Fig. 3.

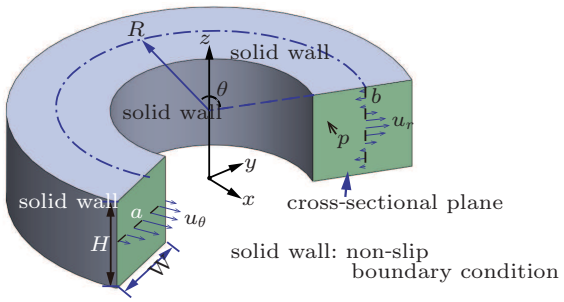


Fig. 3. (color online) Sketch of the annular flow geometry and boundary conditions.

The flow driven by a uniform pressure gradient $\partial p/\partial l = \rho|\boldsymbol{a}|$, streams along the channel circularly, where p is the pressure on fluids, l is the arc length related to position, and $\boldsymbol{a}$ is the acceleration of fluids. By adjusting the acceleration, various Reynolds numbers are set. The secondary flow strength depends on the dimensionless Dean number De, which is defined as $De = Re\sqrt{D_h/2R}$ for the present problem. Re is the Reynolds number defined as $Re = U_m D_h/\nu$, D_h denotes the hydraulic diameter defined as $D_h = 2WH/(W+H)$, U_m is the mean velocity in the channel, and R is the curvature radius. The aspect ratio K of the channel cross-sectional plane is defined as $K = W/H$. In the present work, the channel boundary is set as solid walls, and the bounceback scheme[23] is applied to impose the non-slip boundary condition on the walls.

3.2. Flow structures

We firstly carried out the simulation for a channel of $W = 50$ μm, $H = 50$ μm, $R = 35$ μm under the acceleration $\boldsymbol{a}$ of $2^n \times 10^3$ m/s^2 $(n = 0,1,\ldots,7)$. The fluid density, kinematic viscosity, space step, time step, and relaxation frequency are set as $\rho = 1.0\times10^3$ kg/m^3, $\nu = 1.0\times10^{-6}$ m/s^2, $\Delta x = 1.0\times10^{-6}$ m, $\Delta t = 1.852\times10^{-8}$ s, and $\omega = 1.0/s_\nu = 1.8$, respectively. For simplicity, the simulations are all running with the lattice unit in the present work. We converted the fluid density, kinematic viscosity, and acceleration into lattice units by taking ρ, Δx and Δt as the references. Corresponding to the acceleration range, the simulated Reynolds numbers are 2.34, 4.65, 9.11, 17.16, 30.65, 52.45, 86.15, and 133.89.

Figure 4 is the simulated transformation of flow structure with various Reynolds numbers in the channel, in which the flow remains steady even regardless of different Re. It is shown that: under a lower Re, the flow velocity closes to the inner wall is higher than the flow velocity close to the outer wall; and the boundary layer width near the outer wall is higher than that near the inner wall. That is because the surface area of the inner wall is smaller than the outer wall, and thus the fluid experiences less friction force from the inner wall than from the outer wall. Under almost the same driven force on the cross-sectional plane, the flow intensity near the inner wall becomes stronger than that near the outer wall, as shown in Figs. 4(a)–4(d). As Re is increased to higher values, the flow velocity close to the outer wall becomes higher than the flow velocity close to the inner wall, and the boundary layer near the outer wall tends to become thin and that near the inner wall becomes thick, as shown in Figs. 4(g) and 4(h).

The transformation of flow structures indicates that the fluid in curved channels is not only suffering the viscous force from the wall but also the inertial effect caused by channel curvature. Under a lower Re, the inertial effect is very weak and the viscous force maintains the flow structure's development. As Re is increased higher, the inertial effect will become more obvious. As Re is increased to some critical values, the inertial effect will dominate the flow structure development. In addition, when the fluid flows in the annular microchannel, the pressure near the inner wall is slightly larger than that near the outer wall. The central fluid is thus pushed outwards as a result of the pressure gradient. Meanwhile, the fluid near the top and bottom walls moves inwards in order to satisfy the mass conservation principle. Thus, symmetrically swirling secondary flow vortices arise on the cross-sectional plane. As a result of this, the secondary flow pattern is constructed.

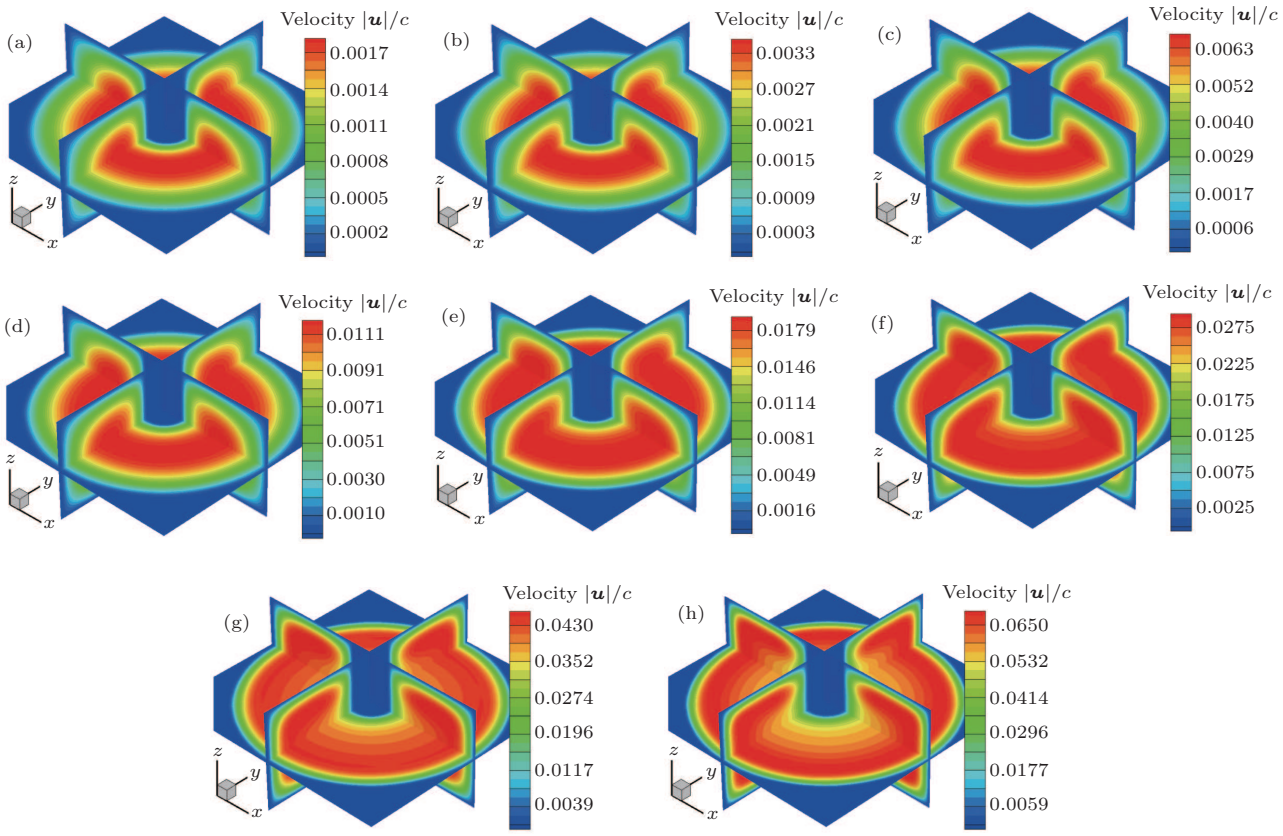


Fig. 4. (color online) Simulated main flow velocity contours at Re = (a) 2.34, (b) 4.65, (c) 9.11, (d) 17.16, (e) 30.65, (f) 52.45, (g) 86.15, and (h) 133.89.

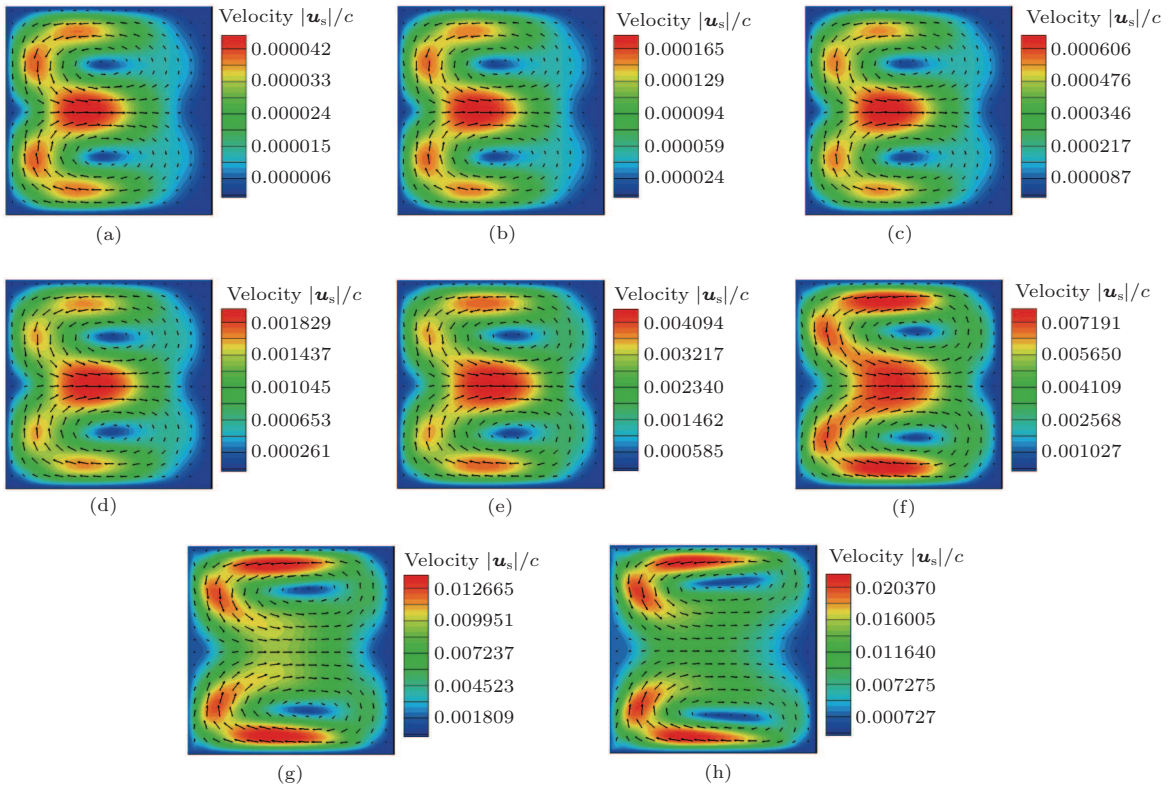


Fig. 5. (color online) Secondary flow velocity contours on the cross-sectional plane of the channel at Re = (a) 2.34, (b) 4.65, (c) 9.11, (d) 17.16, (e) 30.65, (f) 52.45, (g) 86.15, and (h) 133.89.

Figure 5 is the simulated secondary flow vector and intensity distributions in the cross-sectional plane under different Reynolds numbers. Two complex and symmetric swirling Dean vortices were exhibited on both the top and bottom sides of the cross-sectional plane, as stated in reference.[24] It also shows that the maximum velocity comes out at the center of the plane under lower *Re*. As *Re* is increased, both the zero and maximum velocity positions move to the top and bottom walls. In order to quantitatively analysis the flow velocity, we plotted the profiles of axis-round velocity U_θ along the horizontal centerline *a* (on the cross-sectional plane, Fig. 3) and the profiles of radial velocity U_r along the vertical centerline *b* (on the cross-sectional plane, Fig. 3) for various Reynolds numbers, as shown in Figs. 6 and 7, respectively.

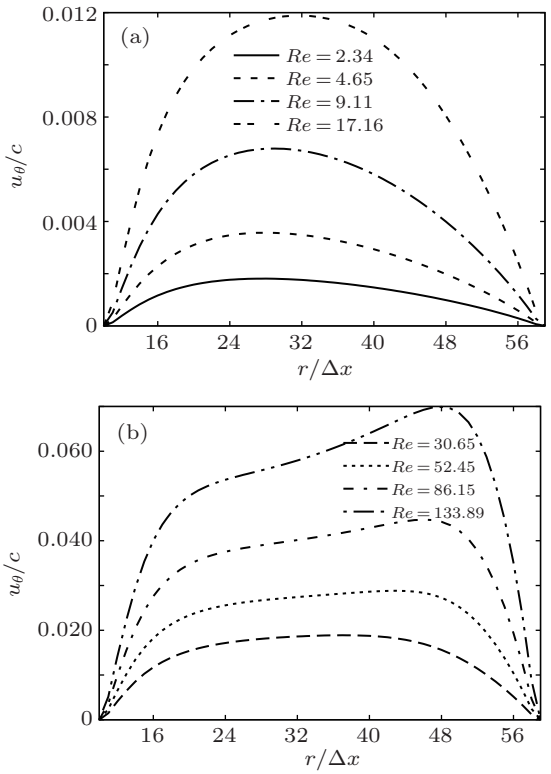


Fig. 6. Axis-round velocity *U* profiles along the horizontal centerline on the cross-sectional plane of the channel at *Re* = (a) 2.34, 4.65, 9.11, 17.16, and (b) 30.65, 52.45, 86.15, 133.89 (*r* is the distance from the point (x, y, z) to *z* axis).

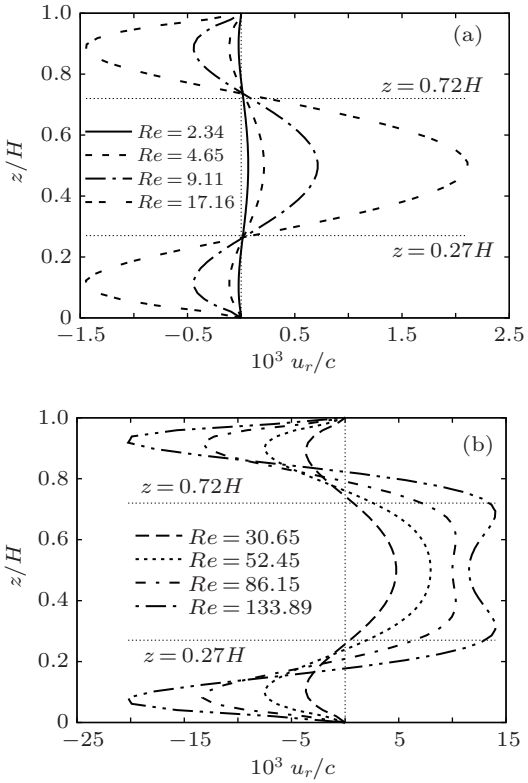


Fig. 7. Radial velocity *U* profiles along the vertical centerline on the channel cross-sectional plane at *Re* = (a) 2.34, 4.65, 9.11, 17.16, and (b) 30.65, 52.45, 86.15, 133.89.

As shown in Fig. 6, the U_θ profiles have similar parabola shapes and the peak velocity lies in the inner side of the channel under the condition of lower Reynolds numbers. When *Re* is increased to 52.45, 86.15, and 133.89, the profile appears wavy and the peak velocity moves to the outer side as shown in Figs. 6(f)–6(h). From Fig. 7, we can see that the zero velocities on the plane are always at the same normalized height of 0.27 and 0.72 at lower Reynolds numbers ($Re = 2.34, 4.65, 9.11, 17.16$) shown in Fig. 7(a). The same conclusion is also reported by Yoon *et al.*[9] However, the zero velocities rule cannot be satisfied when the Reynolds number is increased higher ($Re = 30.65, 52.45, 86.15, 133.89$), as is shown in Fig. 7(b).

It is interesting that the profiles shift from only one peak to two peaks with increasing *Re*, and a valley grows out on the profiles when $Re = 86.15, 133.89$. That is because there is a competition between the viscous and inertial effects on the fluid. Increasing the Reynolds number will result in the inertial effect on the fluid enhancing, but it provides a very limited contribution to the viscous effect comparatively. As *Re* is increased, the vortex in the cross-sectional plane will become more strenuous, and the outwards flowing-trends will be further intensified. Therefore, the maximum zone of the secondary flow velocity disappeared at the center of the cross-sectional plane at $Re = 86.15, 133.89$.

To investigate the effect of the aspect ratio *K* and channel radius *R* on the development of secondary flow structures, simulations are further directed to $K = 3:2, 2:3$ and $R = 35$ μm, 50 μm channel flows with various driven forces. The simulated Reynolds number *Re* and Dean number *De* are listed in Table 2. It can be seen that both *Re* and *De* are increasing with enhancing the pressure gradient. The flow intensity of the cases with $R = 35$ μm is higher than that with $R = 50$ μm under the same pressure gradient and aspect ratio. When the aspect ratio of the channel shifts from 2 : 3 to 3 : 2, both *Re* and *De* are decreased under the same driven force and channel radius. It suggests that the fluids will suffer less driven

force and the flow intensity will be consequently decreased with the increase of K and R. Figure 8 appears the simulated averaged secondary flow velocity $\bar{U}_s$ and the distance d between the symmetrically swirling vortex centers as a function of De. In order to make comparisons among the cases with different channel heights, the vertical coordinates of Fig. 8(b) are normalized by the channel height H. It indicates that both $\bar{U}_s$ and d/H are all enhanced with De increasing. The two figures suggest that the variation tendencies of $\bar{U}_s$ and d/H are significantly influenced by K. The $\bar{U}_s \sim De$ profiles with $K = 2:3$ is higher than that with $K = 3:2$, while the condition of $d/H \sim De$ profiles are on the contrary side. This is also caused by the competition between the viscous and inertial effects in the curved microchannel. When K is lower, the inertial effect on the fluid is more obvious than that under a higher K. The symmetrical secondary vortex centers will become more approaching the geometric center of the cross section. As a result of this, both the averaged secondary flow velocity and the vortex centers distance d/H become higher under a lower aspect ratio. Although the radius will influence the intensity of the main and secondary flows, it contributes nothing to break the balance between the viscous and inertial effects. Hence, the functions of $\bar{U}_s \sim De$ and $d/H \sim De$ are independent of the channel curvature radius R.

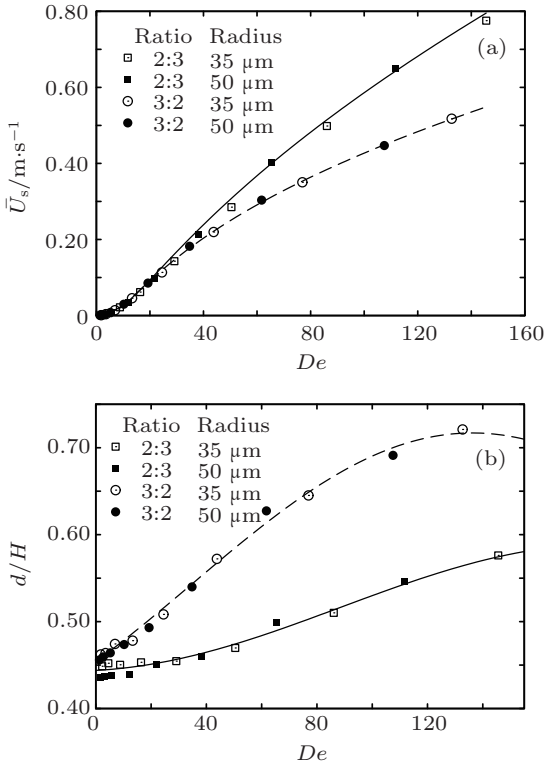


Fig. 8. (a) Averaged secondary flow velocity $\bar{U}_s$ and (b) vortex center distance d on the cross-sectional plane of the channel as functions of Dean numbers (the solid and dashed lines are fitted by the function $y(x) = \exp(a + b/x + c\log_2(x))$).

Table 2. Simulated Reynolds number Re and Dean number De under various driven forces in the channels with $K = 3:2$, $2:3$ and $R = 35$ μm, 50 μm.

$\partial p/\partial l$	$K = 2:3, R = 35$ μm		$K = 2:3, R = 50$ μm		$K = 3:2, R = 35$ μm		$K = 3:2, R = 50$ μm	
10^6 N/m^3	Re	De	Re	De	Re	De	Re	De
1.0	2.767	2.291	2.284	1.583	2.130	1.764	1.910	1.323
2.0	5.479	4.537	4.550	3.153	4.241	3.512	3.816	2.644
4.0	10.613	8.789	8.233	5.704	8.371	6.932	7.580	5.252
8.0	19.737	16.344	11.983	12.025	16.064	13.303	14.789	10.246
16.0	35.161	29.116	31.547	21.856	29.562	24.480	27.799	19.260
32.0	60.902	50.432	55.043	38.135	52.881	43.790	50.220	34.793
64.0	103.951	86.080	94.496	65.469	92.893	76.923	89.066	61.707
128.0	175.794	145.571	161.218	111.696	160.230	132.683	155.180	107.512

3.3. Experimental observation

In order to validate the competition mechanism between the viscous and inertial effects in the curved channel flow, an experimental study was carried out by using a microfluidic device as shown in Fig. 9. A polydimethylsiloxane (PDMS) spiral microchannel was designed and fabricated according to the maskless lithography process. Figure 9(a) illustrates the 5-loops spiral geometry used in the experiment. The microchannel was 150-μm wide and 50-μm high with 400-μm spacing between two neighboring loops. The initial curvature radius of the spiral was 3.5 mm and the total length of the microchannel was 160 mm. The fluid solution consists of deionized water, 1.0 wt% dyed polystyrene particles of 5-μm-diameter (B0200, Thermo Fisher Scientific, Inc.), and 0.5 wt% Tween 20 (Sigma-Aldrich) which can reduce the agglomeration of particles and improve the accuracy of the streamline tracer.

In the experiment, the fluid solution was loaded to the channel via a programmable syringe pump (KDS201, KD Scientific, Inc.) and a short piece of capillary PEEK tubing (1569, Upchurch Scientific) with a constant and precise volumetric flux. The inflow flux was set as 300 μL/min, 600 μL/min, and 900 μL/min in the present study. With the known kinematic viscosity of the fluid $\nu = 1.0 \times 10^{-6}$ m^2/s, the corresponding Reynolds numbers for the 3 cases were draw out, i.e., $Re = 50$, 100, and 150. By taking polystyrene particles as tracing particles, the flow field was photographed and recorded under a fluorescent microscope (IX71, Olympus) and the 14-bit CCD camera (Exi Blue, Qimaging). In order to improve the

precision of the experiment, we overlayed 100 frames of the fluorescent images into one. The gray scale value of the image, which indicates the concentration of tracing particles, was measured by software IMAGEJ (version 1.45s, NIH, USA).

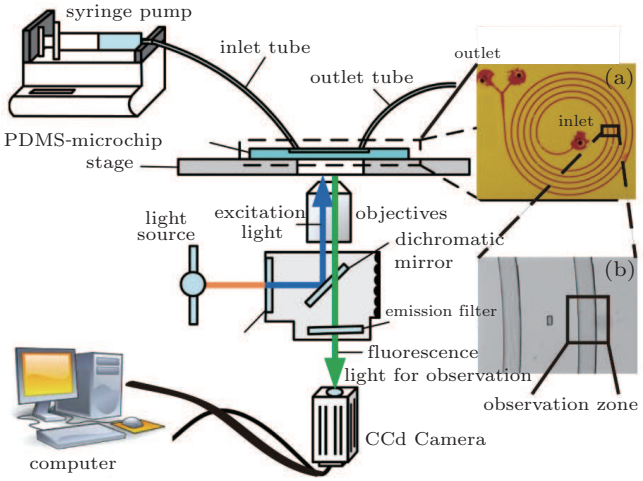


Fig. 9. (color online) Schematic diagram of the experimental microfluidic device. (a) A photomicrograph of the spiral microchannel in the experiment. (b) A partial enlarged view of the spiral microchannel.

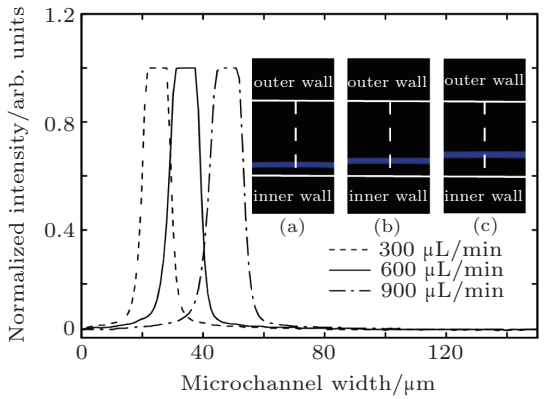


Fig. 10. (color online) Experimental fluorescent images and gray scale profiles scanned along lines perpendicular to the main flow direction under the inflow flux of (a) 300 μL/min ($Re \approx 50$), (b) 600 μL/min ($Re \approx 100$), and (c) 900 μL/min ($Re \approx 150$) (In subfigures, the white scanned lines indicate the approximate position of the spiral microchannel walls, and the white solid lines are the dashed positions).

Figure 10 shows the experimental gray scale profiles scanned along lines (white lines) perpendicular to the main flow direction, and the overlayed fluorescent image under the inflow flux of 300 μL/min ($Re \approx 50$), 600 μL/min ($Re \approx 100$), and 900 μL/min ($Re \approx 150$). The figure shows that the particles were focused into one narrow band along the main flow direction and the bands are all close to the inner channel wall regardless of different Reynolds numbers. That is because the particles in the channel were suffering a couple of forces from the fluid, i.e., the viscous shear induced inertial lift force $\boldsymbol{F}_{\mathrm{L}}$ and the Dean vortices induced drag force $\boldsymbol{F}_{\mathrm{D}}$. The former pushes particles migrating from the center of the channel to the wall, while the latter forces particles to travel within the secondary flow. Particle focusing occurs depending on the relative magnitude of $\boldsymbol{F}_{\mathrm{L}}$ and $\boldsymbol{F}_{\mathrm{D}}$, which reveals the competitive essence between viscous shear and inertial drag effects in the curved channel.

As the forces $\boldsymbol{F}_{\mathrm{L}}$ and $\boldsymbol{F}_{\mathrm{D}}$ vary in magnitude, the exact functional form of this variation is currently unknown. To account for the lift force, Asomolov[25] derived an expression describing the magnitude of the lift forces as a function of the particle position across the channel cross section

$$\boldsymbol{F}_{\mathrm{L}} = \rho G^2 C_{\mathrm{L}}(\boldsymbol{x}, a_p), \tag{15}$$

where G is the shear rate of the fluid which is dependent on the velocity field ($G \sim \nabla \boldsymbol{u}$), C_{L} is the lift coefficient which is a function of position $\boldsymbol{x}$ and particle's radius a_{p}. According to the Stokes drag assumption, the magnitude order of the force $\boldsymbol{F}_{\mathrm{D}}$ exerted on a particle due to secondary flows can then be obtained[26]

$$\boldsymbol{F}_{\mathrm{D}} \sim \rho \bar{U}_{\mathrm{s}}^2 C_{\mathrm{D}}(a_{\mathrm{p}}), \tag{16}$$

where $\bar{U}_{\mathrm{s}}$ indicates the secondary flow intensity and $C_{\mathrm{D}}(a_{\mathrm{p}})$ is the drag coefficient. From these expressions, it is clear that the magnitude of $\boldsymbol{F}_{\mathrm{L}}$ and $\boldsymbol{F}_{\mathrm{D}}$ depends on the distribution of velocities $\boldsymbol{u}_\theta$ and $\boldsymbol{u}_r$ in the present study.

As stated above, the maximum velocity arose close to the outer channel wall under $Re = o(50 \sim 150)$ and the velocity profiles of $\boldsymbol{u}_\theta$ had a parabolic shape. Thus, the shear gradient induced inertial force $\boldsymbol{F}_{\mathrm{L}}$ is directed down the shear gradient toward the walls, and the particles were pushed away from the center to the inner wall under $\boldsymbol{F}_{\mathrm{L}}$. On the other hand, the secondary flow was outwards on the mid-plane in the z direction, and the particles migrate laterally toward the outer wall under $\boldsymbol{F}_{\mathrm{D}}$. The forces are balanced only at the positions near the inner wall. The particle focusing occurs when they reach the equilibrium positions.

Furthermore, the magnitude of $\boldsymbol{u}_\theta$ was increased and the peak of the velocity profile moved outwards with Reynolds numbers increasing. According to Eq. (15), the magnitude of $\boldsymbol{F}_{\mathrm{L}}$ increased with Re increasing. The particles tend to move inwards under the increased $\boldsymbol{F}_{\mathrm{L}}$. However, F_{D} was also increased with Re increasing and it increased faster than $\boldsymbol{F}_{\mathrm{L}}$ ($\Delta \boldsymbol{F}_{\mathrm{D}} > \Delta \boldsymbol{F}_{\mathrm{L}}$) leading to pushing particles outwards. As a result of this, the focusing equilibrium position moved outwards with Re increasing, as shown in Fig. 10. Thus, the inertial effect will become more significant than the viscous effect in the microchannel with Re increasing, which will influence the distribution of flow velocity and force the particle focusing position shift from the inner wall towards the outer wall. All the dynamical behaviors of the fluid and particles in the curved microchannel can be attributed to the competition between the viscous and inertial effects. The experimental results also proved that the MRT–LBM simulated results were reasonable and available.

4. Conclusion

The inertial secondary flow in a curved microchannel was investigated in this paper. We focus the numerical study on the flow structure development and the competition between viscous and inertial effects under various Reynolds numbers.

A 3D MRT–LBM model with a force term applied in this paper was firstly introduced and validated by the simulation of the 3D lid-driven cavity flows. Numerical study on the secondary flow in an annular microchannel was carried out with a range of Reynolds numbers. The simulation results suggest that the secondary flow structures are formed as a result of viscous and inertial competition. The Reynolds number, Dean number, and aspect ratio of cross-sectional plane influence significantly on the competition dynamics and the flow structure development. Both the secondary flow intensity and the normalized vortex center distance are functions of Dean numbers but they are independent of the channel curvature radius. Finally, particle focusing experiments were carried out to validate the competition mechanism, and the experimental observations were qualitatively analyzed with the simulation. It is found that the inertial effect will become more significant than the viscous effect when the Reynolds number is increased.

The present investigations provide an improved understanding of the development of flow structures in curved microchannels, and also demonstrate that the MRT–LBM model is a useful tool in providing physical insights into the underlying mechanism of inertial secondary flow.

Acknowledgment

The authors thank Prof. Zhu Ming-Fang at the Southeast University of China and Dr. Wang Yong at the University of California (Irvine) for their helpful discussion.

References

[1] Gossett D R and Di Carlo D 2009 *Anal. Chem.* **81** 8459
[2] Amini H, Sollier E, Weaver W M and Di Carlo D 2012 *Proc. Natl. Acad. Sci. USA* **109** 11593
[3] McConalogue D J and Srivastava R S 1968 *Proc. R. Soc. Lond. A* **307** 37
[4] Martel J M and Toner M 2012 *Phys. Fluids* **24** 032001
[5] Petitjeans P, Aider J L and Wesfreid J E 1997 *Exp. Fluids* **23** 388
[6] Yang Z X, Cui G X, Xu C X, Zhang Z S and Shao L 2012 *Chin. Phys. Lett.* **29** 054702
[7] Yang W and Zhou K 2012 *Chin. Phys. Lett.* **29** 064702
[8] Ookawara S, Street D and Ogawa K 2006 *Chem. Eng. Sci.* **61** 3714
[9] Yoon D H, Ha J B, Bahk Y K, Arakawa T, Shoji S and Go J S 2009 *Lab Chip* **9** 87
[10] Mao X L, Waldeisen J R and Huang T J 2007 *Lab Chip* **7** 1260
[11] Luo L S, Liao W, Chen X, Peng Y and Zhang W 2011 *Phys. Rev. E* **83** 056710
[12] d'Humières1 D 2002 *Phil. Trans. R. Soc. Lond. A* **360** 437
[13] Kuzmin A, Guo Z L and Mohamad A A 2011 *Phil. Trans. R. Soc. A* **369** 2219
[14] Xu A G, Zhang G C, Gan Y B, Chen F and Yu X J 2012 *Front. Phys.* **7** 582
[15] Zhang J F 2011 *Microfluid. Nanofluid.* **10** 1
[16] Sun D K, Xiang N, Chen K and Ni Z H 2013 *Acta Phys. Sin.* **62** 024703 (in Chinese)
[17] Chai Z H, Shi B C, Lu J H and Guo Z L 2010 *Comput. Fluids* **39** 2069
[18] Boek E S and Venturoli M 2010 *Comput. Math. Appl.* **59** 2305
[19] Chen F, Xu A G, Zhang G C, Li Y J and Succi S 2010 *Europhys. Lett.* **90** 54003
[20] Guo Z L, Zheng C G and Shi B C 2002 *Chin. Phys.* **11** 366
[21] Jiang B N, Lin T L and Povinelli L A 1994 *Comput. Meth. Appl. Mech. Eng.* **114** 213
[22] Wong K L and Baker A J 2002 *Int. J. Numer. Methods Fluids* **38** 99
[23] Maier R S, Bernard R S and Grunau D W 1996 *Phys. Fluids* **8** 1788
[24] Ghia K N and Sokhey J S 1977 *J. Fluids Eng.* **99** 640
[25] Asmolov E S 1999 *J. Fluid Mech.* **381** 63
[26] Di Carlo D, Edd J F, Irimia D, Tompkins R G and Toner M 2008 *Anal. Chem.* **80** 2204